American Mineralogist, Volume 79, pages 274–288, 1994

Short-range order measurements in MgO-FeO and MgO-$LiFeO_2$ solid solutions by DLS simulation-assisted EXAFS analysis

G. A. Waychunas
Center for Materials Research, Stanford University, Stanford, California 94305-4045, U.S.A.
W. A. Dollase
Department of Earth and Space Sciences, University of California, Los Angeles, California 90024, U.S.A.
C. R. Ross II
Bayerisches Geoinstitut, Universität Bayreuth, D-95440 Bayreuth, Germany

Abstract

EXAFS analysis is here used to characterize short-range order (SRO) and local structure in oxide solid solutions by direct measurement of the identity and number of next nearest neighbor (NNN) cations. Precision is improved through the use of constraints, including simulation-derived interatomic distances.

EXAFS Fe-K edge measurements were made on seven MgO-FeO solid solution samples rapidly quenched from 1140 °C. The number of Fe and Mg cations in the NNN shell about an average Fe atom were found to deviate from a random distribution by only 1.4% of total NNN atoms, on average. EXAFS-derived first shell distances agree with simulation results. Fourier deconvolution of Mössbauer spectra of these samples resolves the fine structure, which further supports a random cation distribution.

Computer simulations of α-$LiFeO_2$ and solid solutions of α-$LiFeO_2$ and MgO were carried out for random distributions and for locally ordered distributions in which local charge-balancing cation interchange (simulated diffusion) was permitted. Such interchanges decrease Li-Li and Fe-Fe NNN contacts relative to the number of Li-Fe contacts but do not affect Mg distribution. Fe-K edge EXAFS measurements of two samples of α-$LiFeO_2$ prepared at 1000 °C gave 4.6 and 4.8 NNN Fe atoms, in agreement with the 4.89 predicted by a locally ordered simulation.

Precise fitting of EXAFS spectra of 12 MgO–α-$LiFeO_2$ solid solution samples (also quenched from 1000 °C) required the additional assumption of no Mg atom clustering. EXAFS measurement of the remaining Li,Fe NNN atoms around probe Fe atoms also corresponded closely (within 2.6% of total NNN atoms) to a random distribution. The change from locally ordered to random appeared between 100 and 80% $LiFeO_2$. Several samples with very low Fe content gave erratic results attributable, we believe, to sample heterogeneity.

Introduction

Short-range order (SRO) in a solid solution is the deviation from randomness in pair and higher order correlations. The state of SRO is an important aspect of the internal energy and is a function of the composition, temperature, pressure, and history of the sample. In an n-component solid solution, the state of SRO is quantified by a set of terms, ${}^kP_{ij}$, which are the probabilities of an atom of type i having an atom of type j in any of its kth neighbor equivalent sites (i.e., in one of its kth coordination shell sites). There are n^2 such terms for each coordination shell, of which $n(n-1)/2$ are independent (deFontaine, 1971).

In the MgO-type oxide structures considered here, a cation is surrounded by six nearest neighbor O anions along ⟨100⟩, 12 next nearest neighbor (NNN) cations along ⟨110⟩, eight O anions along ⟨111⟩ in its third coordination shell, six cations along ⟨100⟩ in its fourth shell, and so on. In this paper, we particularly emphasize investigation of the occupancy of the second shell. It is convenient to express the state of order as $S = (P_{FeFe} - X_{Fe})/(1 - X_{Fe})$, where X_{Fe} is the mole fraction of Fe. S is consistent with the Warren-Cowley short-range order parameter (Warren, 1968) and varies from $S > 0$ for a clustered system, to $S = 0$ for a random distribution, to $S < 0$ for ordered arrangements (with a minimum of $S = -1$ for $X = 0.5$). Closely related to SRO is the concept of local configuration, i.e., the detailed interatomic distances and angles resulting from specific atom pair or group interactions, e.g., as might be observed as resulting from charge-coupled substitutions.

Despite its fundamental significance, information on SRO is difficult to obtain because it requires measurement not of average structure, but of local deviation from

0003–004X/94/0304–0274$02.00

average structure. In some cases SRO-type information, such as the number of distinguishable NNN atom configurations, can be obtained from Mössbauer spectroscopic measurements (Osborne et al., 1984; Seifert, 1983; Riedel and Karl, 1980; Steger and Kostiner, 1973; Dowty and Lindsley, 1973). However, Mössbauer applications are usually limited to Fe-containing systems and are severely constrained by uncertainties in resolution and curve-fitting. On the other hand, the technique of extended X-ray absorption fine structure (EXAFS) analysis is well suited to SRO measurements due to the direct effect on EXAFS spectra of the number, type, and distance of neighboring atoms from a (selectable) probe atom. Hence this method can be used to investigate SRO, as well as the geometrical aspects of local configurations, in a wide variety of materials. EXAFS and diffuse X-ray scattering analyses of SRO in Au-Cu alloys have been compared by Claeson and Boyce (1984) and Bessiere et al. (1986). These workers found that the results of the two methods were in good agreement, but that the EXAFS analysis was less precise because of the highly favorable large Z difference for the X-ray measurement. Fe clustering in phyllosilicates has also been studied using polarized EXAFS and compared with results from NMR measurements yielding good agreement (Manceau et al., 1990).

In the present work we apply EXAFS analysis to oxide materials. We have analyzed the composition of the second coordination shell about Fe^{2+} ions in MgO-FeO and about Fe^{3+} ions in MgO–α-$LiFeO_2$ solid solutions. The two systems were chosen as representative of isovalent and heterovalent solid solution series, respectively. The phase α-$LiFeO_2$ has a disordered NaCl structure that is stable above 600 °C. Several ordered NaCl-derived structures can exist at lower temperatures (Hauck, 1980).

Since EXAFS is sensitive to both the atomic number of the backscattering atoms and their distances from the absorber, we can recover these parameters simultaneously, and we report such measurements. These two parameters are not independent, however, since variations in interatomic distances affect the EXAFS phases, whereas variations in atomic number affect both backscattering amplitude and phase. Thus, because of the reasonably strong correlation between these variables, we can markedly reduce our error of measurement by independently fixing one of these parameters. Consequently, we have also simulated the atomic structure of these solid solutions using distance least-squares modeling and have reanalyzed the EXAFS spectra with fixed, model-derived parameters to obtain more precise SRO estimates.

Finally, we have examined the Mössbauer spectra of the MgO-FeO solid solution using high-resolution deconvolution methods and have compared the results of the two types of measurement.

Experimental procedures

Characterization

MgO-FeO samples were prepared in a three-step process (Finnerty et al., 1978). Solutions of metal citrates were mixed in the proper ratio and freeze-dried to produce an intimately mixed fine citrate powder. This material was fired in a muffle furnace at 850 °C for 1 h, producing a finely intermixed oxide powder. Particle size was such that only very broad lines of the MgO structure could be resolved on XRD patterns. This powder was pressed into 0.5-g tablets approximately 2 mm in thickness and heated under controlled atmosphere conditions in a drop-quench furnace for 12 h at 1140 °C. The tablets were quenched by dropping into a H_2O bath. Calculations suggested a quench time of <100 ms at the center of the tablet. The wüstite component of these solutions has stoichiometry dependent on the f_{O_2} within the furnace and the Fe-Mg ratio. End-member wüstite has stoichiometry varying between $Fe_{0.86}O$ and $Fe_{0.95}O$ at 1 atm and 1140 °C, representing Fe^{3+} proportions of about 31 and 9 at%, respectively (Darken and Gurry, 1945, 1946). However, at significant MgO dilutions, the wüstite component is very close to FeO stoichiometry (Phillips and Muan, 1962). In the samples used in this study the reducing atmosphere (Co_2-H_2) was selected to minimize the Fe^{3+} content.

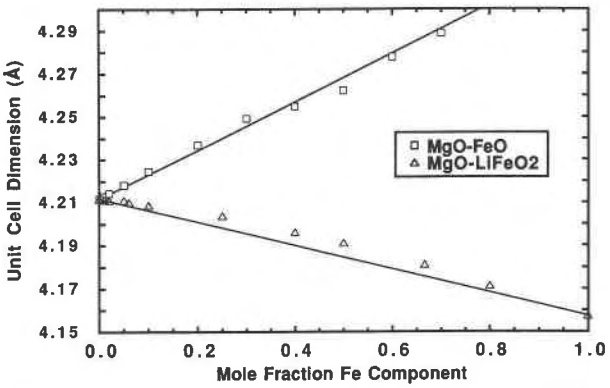

Fig. 1. Cell dimensions of synthetic solid solutions. The 2σ uncertainties are smaller than the data symbols.

MgO–α-$LiFeO_2$ samples were produced by heating tablets of appropriate composition containing reagent-grade Li_2CO_3, MgO, and ferrous oxalate. To offset the loss of Li_2O by sublimation, which leads to the formation of a spinel phase, excess Li_2CO_3 was added. The mixes for the tablets were ground under acetone, allowed to dry, then reground to reduce heterogeneity. Firing was for 6 h in alumina crucibles within a muffle furnace at 1000 °C. Quenching was performed by removing the crucibles from the furnace and placing them in a cool air current. Cooling to room temperature required several minutes. The lowest Fe concentration samples in each series was prepared with 93% enriched ^{57}Fe to aid Mössbauer studies.

All products were examined with X-ray powder diffraction using NBS standard reference material 640*a* (Si metal powder) as an internal standard (a_o = 5.43088 Å). All were of single-phase NaCl structure with narrow line widths. Cell dimensions are shown in Figure 1. Refinement of structure factors was carried out for the MgO-

Table 1. Cell dimensions and compositions of samples

MgO-FeO					MgO–α-$LiFeO_2$				
%Mg	%Fe^{2+}	%Fe^{3+}	a_0 (Å)	Studies	%Mg	a_0 (Å)	Va_0 (Å)*	$(a_0^3 - Va_0^3)$	Studies
99.5	0.5	nil	4.2124(2)	M	99.2	4.2113(2)	4.2111	0.0106	M, E
99.0	1.0	nil	4.2129(2)	M, E	98.0	4.2110(2)	4.2106	0.0212	M, E
98.0	2.0	nil	4.2143(3)	M	95.0	4.2111(2)	4.2089	0.1169	M, E
95.0	4.8	0.2	4.2179(1)	M, E	94.0	4.2102(4)	4.2084	0.0956	M, E
90.0	9.7	0.3	4.2246(4)	M, E	90.0	4.2088(4)	4.2062	0.1380	M, E
80.0	19.6	0.4	4.2369(5)	M, E	75.0	4.2038(3)	4.1981	0.3017	M, E
70.0	29.2	0.8	4.2493(7)	M, E	60.0	4.1962(3)	4.1900	0.3270	M, E
60.0	36.5	3.5	4.2529(4)	M	50.0	4.1912(3)	4.1846	0.3472	M, E
50.0	46.0	4.0	4.2624(5)	M, E	33.0	4.1812(3)	4.1755	0.2985	M, E
40.0	56.0	4.0	4.2778(4)	M	20.0	4.1714(3)	4.1683	0.1617	M, E
30.0	65.1	4.9	4.2898(10)	M, E	0.0	4.1575(3)	4.1575	0.0	M, E

* V = Vegard cell dimension.

FeO samples with the highest Fe content to determine the concentration of $^{[4]}Fe^{3+}$ (Waychunas, 1983).

The samples were examined as powders with the procedures described in Waychunas (1979). No significant variations in Fe-Mg ratio from the fiducial compositions were found in any samples. No detectable Al contamination was observed.

Small aliquots of a representative set of the MgO-FeO samples were dried and weighed, then oxidized in air and reweighed to estimate the original Fe^{3+} content. The method was found to be superior to wet-chemical analysis in both reproducibility and ease and served as a calibration of the Mössbauer analyses. Typical precision was $\pm 0.01 Fe^{3+}/O$.

Mössbauer spectroscopy

Mössbauer analysis of room-temperature and 80-K data were used to determine the Fe^{3+} concentration and site occupation in the MgO-FeO series and to evaluate any electron-hopping processes between Fe^{2+} and Fe^{3+}. Mössbauer spectra of the MgO–α-$LiFeO_2$ series samples were collected at room temperature. Data collection was of sufficient duration that the strongest features had a drop of at least 100 000 counts with respect to the off-resonance background. Sample ^{57}Fe density was typically 0.2 mg/cm^2. Spectra were collected in constant acceleration mode using a Pd source matrix. Velocity calibration was performed with Fe foil, iron oxalate, and sodium nitroprusside standards. Isomer shifts are quoted relative to metallic Fe. Spectral fitting was done with Lorentzian-Gaussian (pseudo-Voigt) lines using a modified version of the Fortran program MOSFT (Dollase, unpublished program). Spectra were fitted with successive models until all constraints could be removed. The χ^2 and Misfit parameters were calculated for all fits.

Spectral deconvolution was accomplished by making a discrete Fourier transform of the raw data and then dividing the resultant complex frequency domain function by the magnitude of the Fourier transform of a normalized Lorentzian line function representing the source energy distribution (Ure and Flinn, 1971; Vinze, 1982). The Lorentzian line used for the deconvolution had a width of 0.10 mm/s, characteristic of the spectral contribution from a nearly perfect source line shape. The resulting complex function was then back-Fourier transformed into the energy domain. Spectra so deconvoluted have higher resolution than normal spectra, but have Fourier ripples in the tails.

Estimation of Fe^{3+} content in the MgO-FeO samples was done using two strategies. Where possible, the spectra were directly fitted and the ratio of Fe^{2+} and Fe^{3+} peak areas was assumed to be equal to the Fe^{2+}-Fe^{3+} ratio. Where individual features were not well resolved or readily located, the mean isomer shift of the entire spectrum was calculated and the Fe^{2+}-Fe^{3+} ratio estimated from that value. Comparison with thermogravimetric results showed a slight bias toward Fe^{3+}, possibly attributable to recoil-free fraction differences. Bias-corrected Fe^{3+} analyses appear in Table 1.

EXAFS data collection and analysis

EXAFS measurements at the Stanford Synchrotron Radiation Laboratory (SSRL) were made on the eight-pole wiggler lines 7-3 and 4-1. Data were collected at room temperature and 80 K and in transmission and fluorescence modes. A dewar system was adapted to an ionization-chamber fluorescence detector to enable low-temperature fluorescence measurements. Most of the analyses were done with the room-temperature transmission data, except for the lowest Fe concentrations, where the room-temperature fluorescence data were used. Comparison of fluorescence and transmission data (collected simultaneously) was done to test for significant self-absorption effects in the fluorescence data. The 80-K data had significantly larger second shell (and fourth shell) amplitudes than the room-temperature data, but a somewhat reduced signal to noise ratio because of the several additional windows in the cryostat. Samples consisted of multiple uniform thin powder layers on cellophane tape with a total absorption factor (μt) of 2 or less.

For all measurements Si (111) monochromator crystals were used to reduce harmonic content in the monochromator exit beam. Detuning of the second crystal was also done according to the procedure of Lytle et al. (1984) to

reduce harmonics further. This detuning resulted in about 50% reduction of the exit beam intensity of the I_0 detector. EXAFS scans were made over the range 7050–8000 eV and repeated at least five times for each sample. Model compounds used to evaluate backscattering amplitude and phase functions were conducted under identical conditions. These model compounds included pure α-Fe_2O_3, $BaFe^{2+}Si_4O_{10}$, $CaFe^{2+}Si_2O_6$, $NaFe^{3+}Si_2O_6$, $LiFe^{3+}Si_2O_6$, $Fe^{2+}Al_2O_4$, and γ-$LiAlO_2$:Fe^{3+}, all of whose structures are known with high precision.

The EXAFS analysis was done as described by Brown et al. (1988), Waychunas et al. (1986), and, in greater detail, by Teo (1986). Spectra were energy calibrated and averaged, then the EXAFS oscillations were extracted by suitable background fitting and subtraction. Representative Fourier transforms of the weighted EXAFS functions are shown in Figure 2. Back-Fourier transforms were taken of the first and second shell peaks in the transforms to produce filtered EXAFS oscillations containing only amplitude and phase information from the first anion and cation shells, respectively. Fitting of these filtered EXAFS functions was done with standard nonlinear least-squares techniques to a plane-wave EXAFS formalism.

EXAFS absorber-backscatter phase and amplitude functions for Fe-Fe interactions extracted from α-Fe_2O_3 were found to be acceptable for all cases. Use of Fe-Fe phases as calculated by Teo and Lee (1979) resulted in larger errors for all models. However, the extracted amplitude function was very similar to the function given by Teo and Lee, except for a scale factor of about 0.6. Fe-Mg phase and amplitude functions were extracted from the $Mg_{0.99}Fe_{0.01}O$ sample and verified through fitting of several model compounds. Fe-O phase and amplitude parameters were extracted from α-Fe_2O_3 and tested by fitting the Fe-O shell in $CaFeSi_2O_6$. For model-compound EXAFS fitting, isotropic temperature factors from X-ray diffraction structure refinements were used to derive estimates of Debye-Waller factors. We used a $\mathbf{k}$ range of 4–12 $Å^{-1}$ for all work. The E_0 value (energy where $\mathbf{k} = 0$) was found to be 3 eV larger in the Fe^{3+} samples than in the Fe^{2+} samples. Once optimized, E_0 values were not varied within any solid solution sample series during refinement.

Initial Debye-Waller factors for EXAFS refinements of the solid solution samples were estimated by adding the interatomic distance variances produced by the simulations and estimated mean-square vibrational amplitudes from γ-$LiFeO_2$, α-$LiFeO_2$, FeO, and MgO from X-ray diffraction structural refinements. In making these estimates it is assumed that changes in SRO have a negligible effect on mean-square vibration amplitude compared with their effect on the variances of interatomic distance.

Computer simulations

Model crystal structures of the present solid solutions were obtained, at representative compositions, by a modified distance-least-squares (DLS) computer simulation

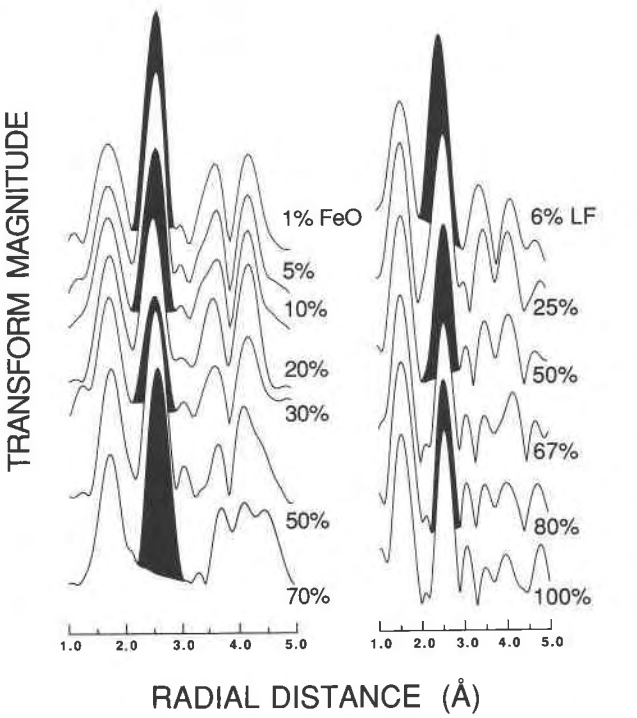

Fig. 2. Representative Fourier transforms of EXAFS data from MgO-FeO and MgO–α-$LiFeO_2$ samples. The second peak containing the second nearest neighbor information has been highlighted to show amplitude changes with composition.

(Meier and Villiger, 1969; Burnham, 1985). The simulation of the isovalent MgO-FeO series has already been described in detail by Dollase (1987). Model interatomic distances and variances for this solid solution were taken directly from that study.

The detailed atomic geometry of a solid solution reflects a competition between (1) a tendency to minimize strain in elements shared between coordination polyhedra (e.g., the length of shared edges) and (2) a tendency for the atoms to achieve local charge balance. The starting model for computation was taken as an MgO-type superstructure, 5 × 5 × 5 unit cells in size, and consisting of 1000 atoms. Relaxation of this structure was carried out sequentially by choosing a nonorigin atom at random and finding the atomic shifts that minimize the sum of the squares of the differences between observed and calculated interatomic distances from this atom to all its surrounding neighbors out to some cutoff distance.

The observational equations expressing the tendency to adopt the average (minimum strain) structure are

$$w(R_{ij} - r_{ij}) = w/r_{ij}\{(x_i - x_j)\delta_x + (y_i - y_j)\delta_y + (z_i - z_j)\delta_z\} \quad (1)$$

where r_{ij} is the distance between atom i at x_i,y_i,z_i and atom j; $\delta_x,\delta_y,\delta_z$ are the atom shifts that are obtained by least-squares solution to the set of observational equations. R_{ij}

TABLE 2. Bond constants used in modeling

Bond	*K* value* (Å)	*K* value** (Å)
Mg-O	1.6995	1.693
Li-O	1.644	1.644
Fe-O	1.768	1.759

* Derived from cell dimensions of end-members.
** From Brown and Altermatt (1985).

are the interatomic distances of the average structure, which are entirely defined by the measured cell dimension, and are applied with weight w. In the models reported here computation was extended to include the 18 nearest neighbors of each atom, i.e., there are 18 equations of type 1 for each atom.

The local charge balancing is applied by an additional six equations, which are obtained as follows: Let b_{ij} be the bond strength (number of pairs of electrons forming a bond) between atoms i and j, and B_i be the sum of bond strengths formed by atom i. In general B_i is unequal to the atom's valence, V_i, because the atom resides in a site for which it is too highly (or weakly) charged, or for which it is too large (or too small) relative to its preferred interatomic distances. In either case all the bonds formed by atom i are probably too weak or too strong, and so there exists a scaling factor to be applied to all bonds that would bring their sum as close as possible to the atomic valence (i.e., charge balance). This scaling factor is V_i/B_i, or if simultaneous charge balance on both atom i and j is considered, it is V_iV_j/B_iB_j.

Applying this scale factor to the current bond strength, b_{ij}, gives the bond strength needed to obtain charge balance, $b_{ij}V_iV_j/B_iB_j$. This optimum bond strength can then be transformed to the ideal distance, D_{ij}, needed to produce charge balance by the relationship between bond length and bond strength, such as that given by Brown and Altermatt (1985) as

$$b = \exp[(K - r)/0.37] \tag{2}$$

where b is the bond strength, r is the bond length, and K is a constant for each type of bond. Hence we obtain

$$D_{ij} = K - 0.37 \ln[b_{ij}V_iV_j/B_iB_j]. \tag{3}$$

The additional six observational equations that apply the charge balancing tendency (with unit weight) are then

$$\begin{aligned} D_{ij} - r_{ij} &= -0.37 \ln[V_iV_j/B_iB_j] \\ &= 1/r_{ij}\{(x_i - x_j)\delta_x + (y_i - y_j)\delta_y \\ &\quad + (z_i - z_j)\delta_z\}. \end{aligned} \tag{4}$$

The resulting 24 equations (Equations 1 and 4) are solved by least-squares for the atom shifts, which are applied to atom i. Then another atom is chosen at random and the process is repeated. After an average of 50 iterations per atom all atomic shifts are $\ll 10^{-4}$ Å, which is adequate convergence for our purposes. The atomic positions are then examined to determine interatomic distance means and variances.

The parameters used in this model are the cell dimension, the bond strength parameters for Mg-O, Fe-O, and Li-O bonds, and the relative weight assigned to each of the two competing tendencies. The cell dimension is obtained from independent X-ray measurements of the synthetic samples reported in Table 1 and Figure 1. Because of the simple relation between bond length and cell dimension in the MgO structure, the bond strength values, K, may be calculated from Equation 2, assuming that the atoms are perfectly charge balanced in the pure end-member compounds. The K values so obtained (Table 2) are in relatively close agreement with those obtained by fitting to hundreds of crystal structure determinations by Brown and Altermatt (1985).

The final, and only adjustable, model variable, w, determines the relative importance of conforming to the overall average MgO-like arrangement compared with the charge-balancing tendency of unit weight. Simulations made with a small value of w result in an almost perfectly charge-balanced structure, but one with extreme local distortions leading to highly implausible interatomic distances, such as O-O distances of 2.4 Å. The larger the value of w, the more rigid and locally undeformable the structure becomes. The value of $w = 0.1$ was selected based on a comparison with previous modeling studies and EXAFS results (Dollase, 1980, 1987) and is further supported below.

There are several advantages of this solid solution modeling method that may be pointed out. It relieves the modeler of the problem of choosing the optimum distances, it is equally applicable to isovalent and heterovalent solid solutions, and it automatically includes many-body interactions. That is, the final atomic positions are not just the result of several fixed pairwise interactions, but rather the result of pairwise interactions that themselves depend upon additional nearby atom locations, distances, bond strengths, and charge balances.

The modeling described above employs fixed random distributions of the substituent cations. It is also possible to interchange pairs of randomly selected cations when such an interchange moves ${}^kP_{ij}$ in the desired direction and to halt the interchange process at some desired degree of SRO. This was done in the case of the MgO-FeO series. For the MgO–α-$LiFeO_2$ series, partially ordered models were produced by the interchange of randomly selected cation pairs, if the interchange reduced local charge imbalance around both sites. Such a procedure converges rapidly to what is here called a locally ordered configuration such that there are no further interchanges possible (in this finite model) without increasing local charge imbalance. The degree of SRO was then evaluated using a Monte Carlo method.

RESULTS

MgO-FeO

First shell analysis. The mean interatomic distances from the probe Fe atoms to the six surrounding O atoms

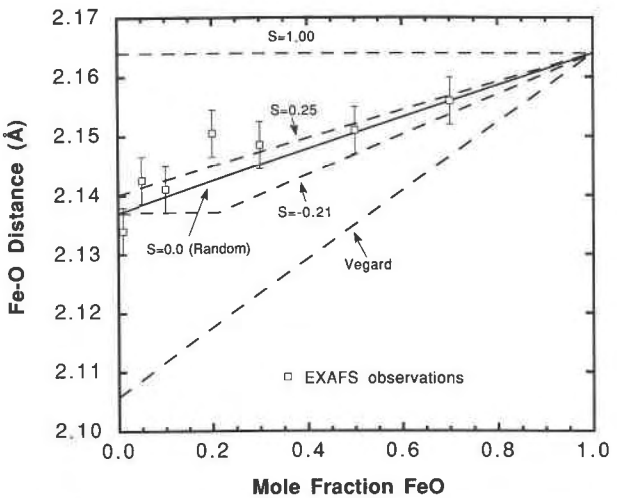

Fig. 3. Interatomic distances from computer simulations compared with EXAFS results for MgO-FeO. $S = 0.0$ for random atom arrangements, and positive or negative for clustered or ordered arrangements, respectively. Error bars indicate $2\sigma = 0.004$ Å from least-squares fitting. Typical EXAFS systematic errors can be about 0.01 Å.

TABLE 3. First shell EXAFS results

MgO mol%	Fe-O distance (Å)	σ^2 (Å^2)	FF*
	MgO-FeO		
99.0	2.156 (0.002)	0.0036	0.033
95.0	2.151	0.0036	0.061
90.0	2.148	0.0036	0.113
80.0	2.150	0.0036	0.255
70.0	2.141	0.0036	0.040
50.0	2.142	0.0036	0.087
30.0	2.134	0.0036	0.112
	MgO–α-LiFeO$_2$		
0.00	2.046 (0.002)	0.0113	0.225
0.00	2.044	0.0120	0.062
20.0	2.042	0.0091	0.077
20.0	2.052	0.0110	0.130
33.3	2.051	0.0101	0.058
50.0	2.053	0.0105	0.076
60.0	2.062	0.0102	0.097
75.0	2.057	0.0102	0.117
90.0	2.057	0.0135	0.114
94.0	2.069	0.0056	0.319
95.0	2.061	0.0089	0.225
98.0	2.068	0.0080	0.197
99.2	2.067	0.0093	0.147
99.2	2.064	0.0089	0.432

* FF = fitting function value, in this case $\frac{1}{N}\Sigma(\text{obs}_i - \text{calc}_i)^2$, where obs and calc refer to values of the observed and calculated back-transform EXAFS contributions from the second neighbor shell.

of the first neighbor shell, as obtained from the EXAFS analysis, are shown in Figure 3 and Table 3. For comparison, mean (Fe,Mg)-O bond lengths calculable from the cell dimension trend and Fe-O bond lengths furnished by the simulation procedure are also shown for several states of order. Note that the observed Fe-O distances are far from the mean cation to O (Vegard) distances except for the pure FeO composition. For a random distribution, the simulation-derived Fe-O distance extrapolates to 2.136 Å in pure MgO. This distance is about halfway between what might be regarded as the ideal Fe-O distance found in stoichiometric FeO (2.164 Å) and the Mg-O distance found in MgO (2.106 Å), and it reflects the fact that the sixfold-coordinated NaCl structure allows about 50% bond-length adaptation or compliance (Dollase, 1980).

The effect of clustering (increased preference of Fe atoms for Fe neighbors) is to rotate the Fe-O distances shown in Figure 3 clockwise around the Fe-O distance in FeO. The effect of ordering (alternation) is to rotate the trend in the opposite direction. At the most extreme ordering, Fe atoms would have only Mg next nearest neighbors yielding a constant Fe-O distance, up to a compositionally controlled limit, above which there is a linear trend to pure FeO (see Fig. 3).

Within the measurement uncertainty, there is good agreement with the bond lengths calculated for a state of order, S, equal to 0 (random solid solution) to around 0.25 (slightly clustered). The more direct measure of SRO obtained from EXAFS analysis of the second shell (discussed below) confirms a value of $S = 0$ within experimental uncertainty. The agreement of the measured Fe-O distances with those calculated by the simulation methods may be taken as further confirmation of the choice of weighting factor discussed above in the simulation methods section.

The Debye-Waller factors extracted from the EXAFS analysis were smaller than estimates based on X-ray thermal parameters. Using $B(O) = 0.33$ and $B(Mg) = 0.296$ (Barron, 1977) for MgO, and $B(O) = 0.79$ and $B(Fe) = 0.45$ Å^2 (Koch and Cohen, 1969) for $Fe_{1-x}O$, we calculate EXAFS Debye-Waller factors of 0.0055–0.0110 Å^2 over the solution series. These values are maximal ones, as the calculation assumes no correlated motion between absorber-backscatterer pairs, though that certainly occurs. However our fitted Fe-O shell Debye-Waller values averaged 0.0036 Å^2 and were fixed to this value in the final refinement. A systematic decrease could be due to the use of α-Fe_2O_3 as the Fe-O model compound from which amplitude information was extracted. Also the Koch and Cohen (1969) B values are for a wüstite with stoichiometry $Fe_{0.905}O$, which has much more Fe^{3+} and related defect concentration than occurs in the wüstite component in our solutions. On the other hand, the computer modeling suggested no significant change in Fe-O bond-length variance across the solid solution, which is consistent with our results.

Second shell analysis. It is possible to obtain second shell Mg-Fe compositions by several types of analysis of the filtered second shell EXAFS spectra: (1) The total integrated amplitude as manifested by the area under the second shell structure function peak can be modeled. (2) The amplitude function of the second shell can be extracted with the complex back transform and fitted by a model with varying Fe-Mg ratio. (3) The phase function of the second shell can be similarly fitted. (4) Both phase and amplitude can be refined simultaneously. In the case

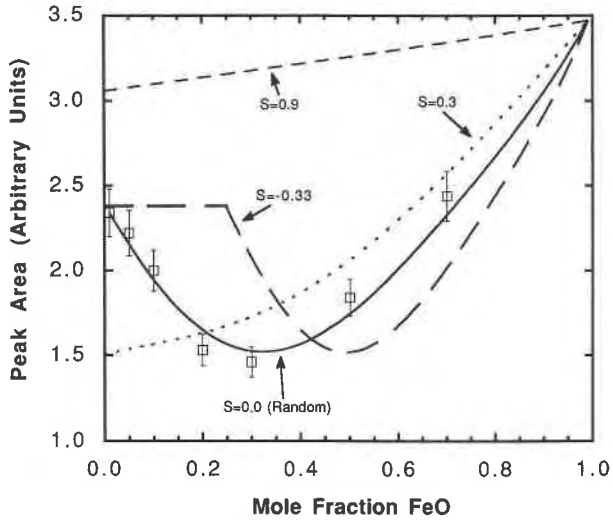

Fig. 4. Calculated vs. observed second shell peak areas in the Fourier transform of MgO-FeO samples. The $S = 0.9$ line and $S = 0.3$ curve decrease and increase, respectively, to 2.37 area units in the near vicinity of 0.0 mole fraction FeO. Error bars on the observed data points indicate 2σ.

of the MgO-FeO solutions, approaches 1 and 2 work with about the same degree of precision, since there are large changes in the second shell backscattering amplitude and phase as Mg substitutes for Fe^{2+} and thus significant changes in the second shell transform peak area as well (Fig. 2). Case 3 yields larger uncertainties because of the relatively smaller change in phase compared with amplitude between Fe^{2+} and Mg backscattering. Case 4 yields the best results, perhaps as expected, as it includes significant variations in both phase and amplitude between Fe^{2+} and Mg. The extracted second shell peak areas are compared in Figure 4 with calculated areas representing various degrees of SRO. In Figure 5 we show an example of simultaneous fitting of phase and amplitude, i.e., modeling the complete back transform, for the composition $Mg_{0.8}Fe_{0.2}O$. The individual contributions from Mg and Fe backscattering are shown in the bottom part of Figure 5.

The refinements are carried out with the constraints of constant total second shell cation occupation equal to 12, and no occupation allowed to become negative. Fitting errors approximately double in magnitude, without the full occupancy constraint, whereas without the positive occupation constraint, the number of Fe next nearest neighbors becomes slightly negative at lowest Fe concentrations. Fe-Mg,Fe distances were fixed to those predicted by the simulations during occupancy refinement. Use of simulation-derived distances for solutions with $S = 0.25$ and $S = -0.21$ gave occupancy results that were inconsistent with clustering and ordering, respectively. Use of simulation distances for $S = 0.0$ yielded consistent results. The resulting second shell occupancies are given in Table 4 and shown in Figure 6. The measured number of Fe,Mg NNN atoms deviates from a random distribution ($S = 0.0$) by only 1.4% of total NNN atoms, on average, over the entire solid solution range. In Figure 6 two plausible ordering schemes are also depicted. The CuAu-type ordering refers to the tendency to have alternating (100) planes of Mg and Fe atoms. The completely ordered structure would have a NNN configuration of 4Fe and 8Mg about a given probe Fe, and 4Mg and 8Fe about a given Mg. This ordering scheme cannot continue at compositions having >50% FeO. The Cu_3Au-type ordering has alternating (100) planes of composition $Mg_{0.5}Fe_{0.5}$ and $Mg_{1.0}$. Thus the ordered structure would have 2Fe and 10Mg about a given probe Fe. This ordering provides maximum exclusion of Fe NNN about the probe Fe up to $Mg_{0.75}Fe_{0.25}O$, and at higher FeO content the solution follows a $S = 0.33$ ordering trajectory.

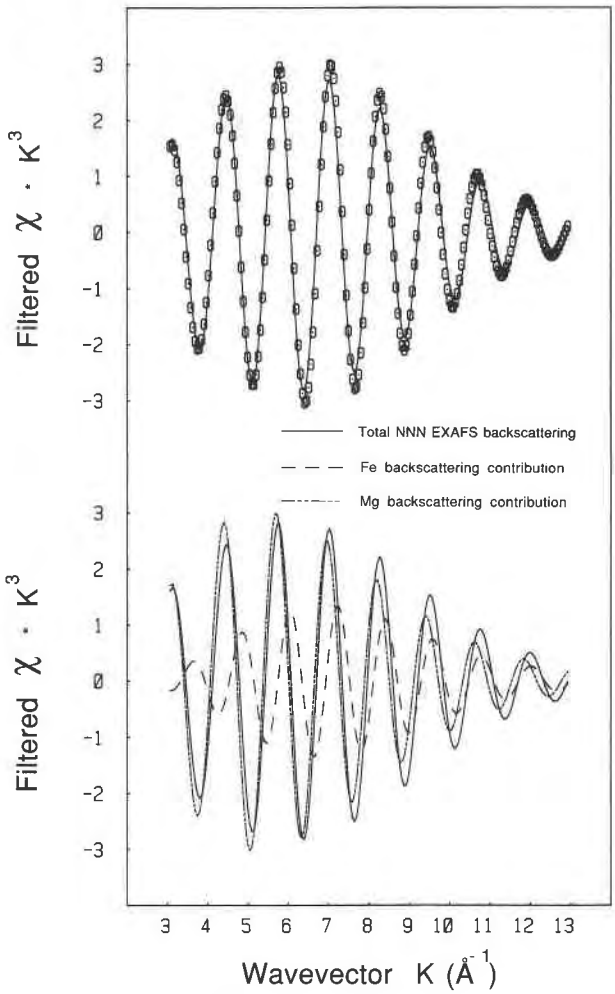

Fig. 5. Representative fit to filtered second shell EXAFS from $Mg_{0.8}Fe_{0.2}O$. (**Top**) calculated points (open circles with dot), filtered EXAFS data (solid line). (**Bottom**) filtered data (solid line) with calculated Mg (dot-dashed line), and Fe (dashed line) backscattering contributions. Note better agreement with observations for the Mg component at low **k** and for the Fe component at high **k** due to the greatly different backscattering amplitude functions for these atoms.

TABLE 4. Second shell EXAFS results

MgO mol%	MgO-FeO No. Fe NNN* Observed	Random	Difference	σ^2 (Å^2)	FF
99.0	0.00	0.12	−0.12	0.0057	0.128
95.0	0.50	0.60	−0.10	0.0057	0.302
90.0	1.03	1.20	−0.17	0.0057	0.153
80.0	2.30	2.40	−0.10	0.0057	0.161
70.0	3.64	3.60	0.04	0.0057	0.196
50.0	6.40	6.00	0.40	0.0057	0.106
30.0	8.62	8.40	0.22	0.0057	0.130

MgO mol%	MgO–α-$LiFeO_2$ No. Mg NNN**	No. Fe NNN	No. Li NNN†	Li-Fe	σ^2 (Å^2)	FF
0.00	0.00	4.61	7.39	1.60	0.0104	0.020
0.00	0.00	4.81	7.19	1.49	0.0104	0.024
20.0	2.40	4.57	5.03	1.10	0.0064	0.073
20.0	2.40	5.14	4.46	0.87	0.0064	0.014
33.3	4.00	3.96	4.04	1.02	0.0064	0.036
50.0	6.00	3.19	2.81	0.88	0.0064	0.029
60.0	7.20	2.31	2.49	1.08	0.0064	0.186
75.0	9.00	1.85	1.15	0.62	0.0064	0.087
90.0	10.8	0.45	0.75	1.67	0.0064	0.097
94.0	11.28	0.03	0.69	—	0.0064	0.378
95.0	11.40	2.05	—	—	0.0064	0.053
98.0	11.76	0.06	0.18	—	0.0064	0.896
99.2	11.904	0.00	0.096	—	0.0064	0.093
99.2	11.904	0.60	—	—	0.0064	0.477

* About average Fe atom.
** Assumed from bulk composition.
† Obtained by difference.

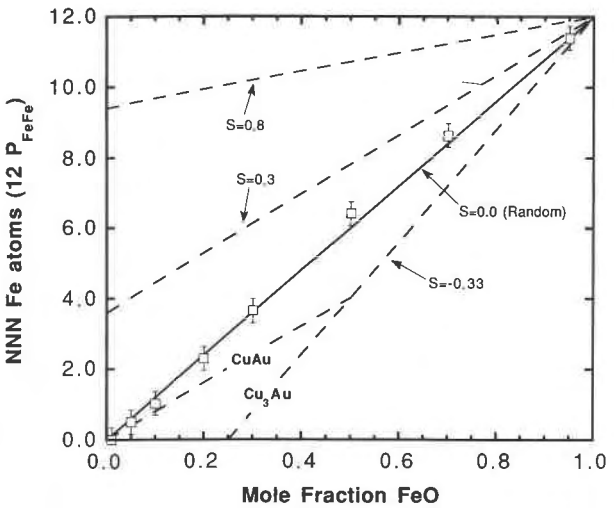

Fig. 6. Results of refinements of filtered second shell EXAFS for the MgO-FeO system. The CuAu and Cu_3Au lines refer to Mg-Fe cation ordering consistent with these ordered structures. The $S = 0.8$ and $S = 0.3$ lines fall to 0.0 NNN Fe atoms in the near vicinity of 0.0 mole fraction FeO. The Cu_3Au ordering line ($S = -0.33$) is constant at 0.0 NNN Fe atoms below 0.25 mole fraction FeO.

Debye-Waller values for all second shell fits averaged 0.0057 Å^2 and were fixed to this value in final refinements of the NNN occupancies. The predicted maximum Fe-Fe,Mg Debye-Waller values from the B values noted above are 0.0053–0.0079 Å^2. The closer agreement between estimated and observed Debye-Waller values, relative to the first shell case, suggests much less correlated motion between Fe-Mg,Fe pairs than between Fe-O pairs, which is reasonable. The modeling indicated, as with Fe-O distances, that no significant change in Fe-Fe,Mg distance variance should occur across the solution.

Mössbauer analysis. Liquid N_2 temperature spectra of MgO-FeO solution samples are shown in Figure 7. Because all of the samples were synthesized with minimal Fe^{3+} content, only samples with >40% FeO have significant Fe^{3+} component. There is a continuous change in the shape of the spectra with increasing FeO component. The lowest FeO compositions show essentially a singlet absorption. This envelope broadens to a narrowly split doublet and then to a gradually widening doublet as FeO content increases. Because the increase in quadrupole splitting is due to dissimilarity in next nearest and more distant neighbors, at compositions beyond 50% FeO there should be a reversal of this process. If Fe^{3+} is neglected, the neighbor environment then becomes progressively more symmetrical. Such a trend is consistent with the Mössbauer spectrum of reduced wüstite from a disproportionation process (Hentschel, 1970), which shows a singlet.

Definite substructure appears in these spectra. At about 20% and greater FeO content the spectrum appears to be composed of two incompletely resolved wide doublets. This appearance prompted Kurash et al. (1971) to fit two broad doublets to their 80-K spectra and assign the inner and outer doublets to the surface and core sites, respectively, of FeO clusters in the solid solution.

Because the Mössbauer spectral envelopes are broad, a large number of individual Lorentzian lines of standard width would be necessary to fit them well. More importantly, no resolved features are present in the spectra to indicate individual doublet or singlet line positions or to serve as a control on line areas. Hence many fitted lines with many attendant possible fit combinations could describe the fitted envelopes but not result in a unique spectral interpretation. Because of this, we attempted to enhance spectral resolution by the Fourier deconvolution operation noted earlier. We chose to use the liquid N_2 temperature spectra because the enhanced quadrupole splittings might reveal additional detail. These deconvoluted spectra are shown in Figure 8. Because of the deconvolution process, the Lorentzian component of the Mössbauer spectrum is reduced substantially. Hence all fitted lines had a large Gaussian component. It should be emphasized that the result of the deconvolution is, barring imperfections in the deconvolution, a representation of the distribution of Mössbauer absorbers. Therefore, there is no specific theoretical shape to be used in fitting these profiles. For simplicity, a pseudo-Voigt function was used. The shape that best fitted the lowest FeO concentration sample was used throughout the fitting procedures (80% Gaussian, 20% Lorentzian).

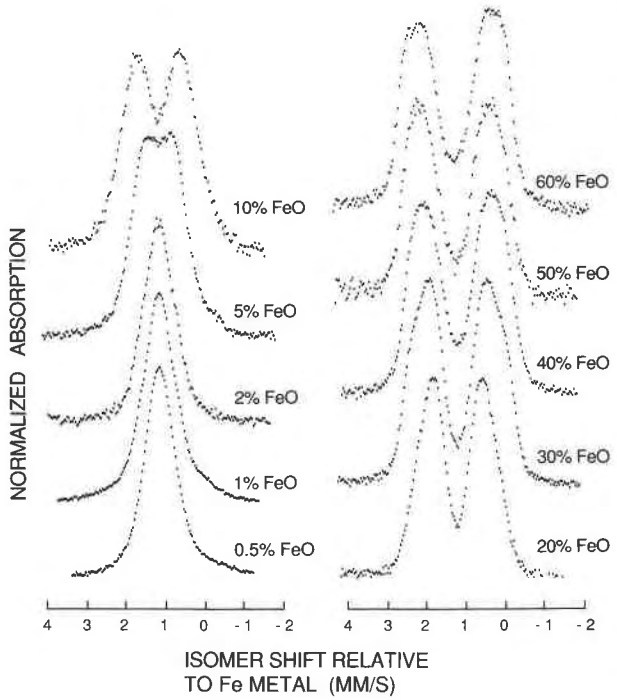

Fig. 7. MgO-FeO Mössbauer spectra at 80 K.

The ½% FeO spectrum was narrowed by the deconvolution process, but no new features appeared. The deconvoluted spectrum could be fitted by a single narrowly spaced doublet, or by various combinations of such a doublet with a small outer doublet. The area ratio between these doublets was very sensitive to line shape. The deconvoluted 1% FeO spectrum, in contrast, clearly showed the presence of an additional outer doublet. The two doublets could be fitted with relatively small uncertainties in the line positions. The deconvoluted 2% FeO spectrum showed an enhancement of this second doublet by almost a factor of two, if the assumption is made that the line positions changed little with composition. Computation of the probabilities of Fe^{2+} association in a random solution (Table 5) are consistent with assignment of the inner doublet to isolated Fe^{2+} (no Fe^{2+} NNN or fourth NN) and the outer doublet to Fe^{2+}, with an Fe^{2+} in either the NNN or fourth NN position. This assignment agrees well with the ratio of the areas of the fitted doublets, if some variation in line widths is permitted.

The deconvoluted 5% FeO spectrum can also be fitted well with this random occupation model, although a third doublet with larger quadrupole splitting is now necessary. The area of this doublet is consistent with its assignment to Fe^{2+}, with two neighboring Fe^{2+} ions distributed among some combination of the NNN and fourth NN sites. The area ratios of the three inner doublets agree well with random probabilities and with the positions of fitted lines to the 5% FeO spectrum. For example, the proportion of isolated Fe^{2+} based on the Mössbauer fits is 92, 80, 69, and 37% for the samples having 99.5, 99.0, 98.0, and 95 mol% MgO, respectively. The random probability model yields 91, 83, 69, and 40% for the same cases. We continued this fitting procedure with the 10% FeO deconvoluted spectrum, with acceptable results. An additional fourth outermost doublet must be added, presumably to accommodate configurations of Fe^{2+} with three or more Fe^{2+} neighbors. The fit results are compiled in Table 6.

Table 5. NNN and fourth NN random occupation probabilities for MgO-FeO solid solutions

Configuration		MgO mol%				
NNN	4th NN	99.5	99.0	98.0	95.0	90.0
0	0	0.914	0.834	0.695	0.397	0.150
1	0	0.055	0.101	0.170	0.251	0.200
0	1	0.027	0.051	0.085	0.125	0.100
1	1	<0.01	<0.01	0.0208	0.079	0.133
2	0	≪0.01	<0.01	0.0190	0.0725	0.122
2	1	≪0.01	≪0.01	<0.01	0.0229	0.0814
0	2	≪0.01	≪0.01	<0.01	0.0164	0.0277
1	2	≪0.01	≪0.01	<0.01	0.0104	0.0370
2	2	≪0.01	≪0.01	≪0.01	<0.01	0.0226
Σ 2/0; 0/2; 2/1; 1/2; 2/2		<0.01	<0.01	0.0256	0.1252	0.2909

For greater FeO content, we expect the new fourth doublet to increase in area. This would increase the observed splitting of the full envelope, which is observed, as shown in Figures 7 and 8. Because of the many geometric configurations of three or more Fe^{2+} cations, it is clear that only with increasingly arbitrary assumptions could we continue to analyze the higher FeO content samples in this way. However, the important point is that the Mössbauer results show a change in spectral shape with composition that is consistent with random neighbor associations and show good quantitative agreement with prediction for the lower Fe content samples, where more complete analysis is possible. As a further test of this, fits to the deconvoluted spectra based on significant clustering were attempted. Major clustering ($S = 0.6$–0.9) results in similar Fe^{2+} neighbor configurations independent of composition. Minor clustering ($S = 0.3$) produces two and three NNN Fe^{2+} configurations at very low overall bulk compositions. Such fitting failed to produce the spectral changes that are observed, even with significant variations in subcomponent peak shapes and positions. Hence the low FeO composition Mössbauer results in particular and all Mössbauer results in general best support a random distribution model.

Fe^{3+} in MgO-FeO solid solutions

Although the amount of Fe^{3+} (see Table 1) is small, especially in the low-Fe samples, it is necessary to consider what effect, if any, its presence has on our results. Previous analysis of the Mössbauer spectra of related samples (Waychunas, 1983) has shown that the Fe^{3+} resides mainly on octahedral sites along with charge-compensating vacancies, corresponding to the replacement $3Fe^{2+} = 2Fe^{3+} + \square$. The effect of the Fe^{3+} on the first shell is to introduce a small fraction of Fe^{3+}-O distances

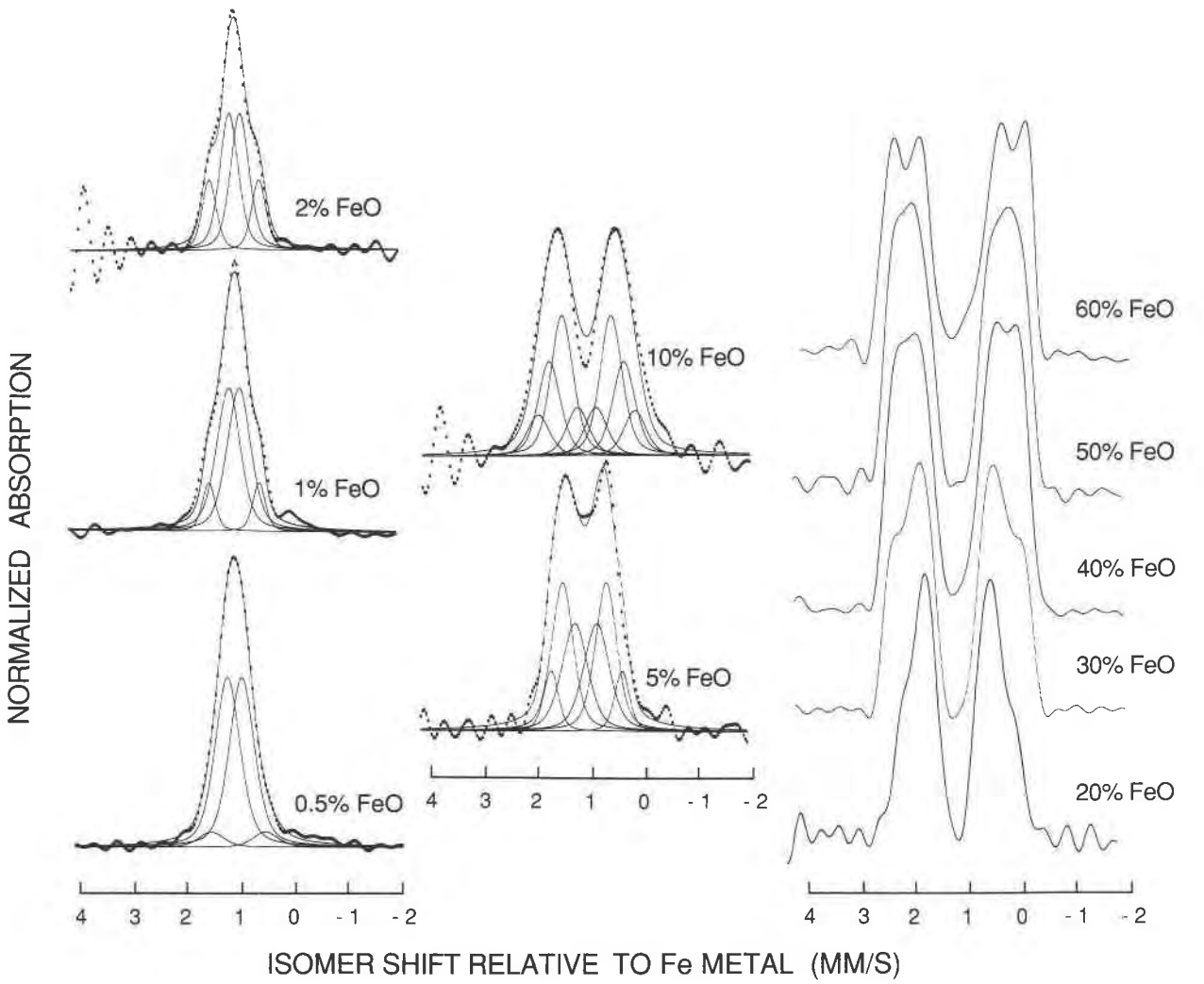

Fig. 8. Deconvoluted 80-K Mössbauer MgO-FeO spectra with component fitting.

shorter than the Fe^{2+}-O distances by about 0.1 Å. However, such a contribution could not be detected in attempted EXAFS refinements using separate near neighbor shells. In the second shell, the presence of a small fraction of vacancies alters the total number of backscattering cations, and thus the measured peak areas or amplitudes need to be renormalized. For example, the 30% MgO sample has the composition $Mg_{0.30}Fe^{2+}_{0.638}Fe^{3+}_{0.046}\square_{0.023}O_{1.000}$, with all species assumed octahedral. The Mg-Fe ratio of this composition vs. one with no Fe^{3+} ($Mg_{0.30}Fe^{2+}_{0.70}O_{1.00}$) only differs by a few hundredths of 1%. The second shell EXAFS refinements are primarily affected by changes in the ratio of these backscattering species. Hence this degree of oxidation cannot be seen directly in the EXAFS results.

A small fraction of $^{[4]}Fe^{3+}$ has different consequences. A larger proportion of cation vacancies would be expected. One additional such vacancy must occur for each Fe^{3+} shifting from octahedral into tetrahedral coordination. If all Fe^{3+} were tetrahedrally coordinated, then the concentration of accompanying cation vacancies would produce a significant reduced Fe backscattering relative to the unoxidixed composition. The maximum effect would cause an increase in the Mg-Fe ratio, as determined by EXAFS, by about 6%. Previous study of $^{[4]}Fe^{3+}$ in MgO-FeO-Fe_2O_3 solutions demonstrated that the fraction of Fe^{3+} in tetrahedral coordination is expected to be about 25% (Waychunas, 1983). This leads to an effect of, at most, about 1.5%, which is within the estimated error of our NNN determinations. Our EXAFS results actually show deviations from the random model in the opposite direction for the 50 and 30% MgO samples. This latter effect could be due to the clustering of cation vacancies and Fe^{3+} ions and is considered below.

α-$LiFeO_2$

First shell analysis. EXAFS analysis of the first shell mean Fe^{3+}-O distances yield 2.044 and 2.046 (±0.004)

TABLE 6. Mössbauer results

		MgO–α-$LiFeO_2$						
MgO mol%		99.2	94.0	90.0	75.0	75.0	60.0	60.0
Doublet 1	IS*	0.354	0.347	0.360	0.348	0.348	0.351	0.351
	QS*	0.483	0.426	0.471	0.477	0.390	0.557	0.439
	Area	1.000	1.000	1.000	1.000	0.520	1.000	0.485
Doublet 2	IS					0.348		0.351
	QS					0.653		0.736
	Area					0.480		0.515
	Width**	0.340	0.316	0.313	0.257	0.177/0.278	0.290	0.189/0.311
	χ†	3.11	1.96	3.33	3.91	2.49	4.27	2.72
	M	1.922	0.759	2.218	2.600	1.041	3.016	1.202
	ΔM	0.161	0.079	0.182	0.191	0.091	0.215	0.100
		MgO-FeO						
MgO mol%		99.5	99.0	98.0	95.0	90.0		
Inner Doublet	QS	0.253	0.186	0.189	0.385	0.321		
	Area	0.919	0.801	0.688	0.373	0.149		
	Width	0.522	0.490	0.386	0.540	0.463		
Doublet 2	QS	0.963	0.988	0.872	0.775	0.868		
	Area	0.081	0.199	0.311	0.469	0.433		
	Width	0.522	0.257	0.296	0.450	0.463		
Doublet 3	QS				1.259	1.319		
	Area				0.157	0.290		
	Width				0.309	0.463		
Doublet 4	QS					1.673		
	Area					0.127		
	Width					0.463		
	χ	0.71	1.42	3.73	1.99	3.99		
	M	0.118	0.500	3.452	0.591	2.135		
	ΔM	0.035	0.067	0.299	0.057	0.143		

Note: for MgO-FeO, all IS values constrained to 1.147 mm/S relative to ^{57}Fe in Fe metal.
* Units in millimeters per seconds.
** Full width at half maximum.
† Standard reduced χ^2 formulation.

Å for the two samples measured. These values are close to the 2.048 Å mean distance predicted for a locally ordered model. The random distribution model mean distance is, however, only very slightly longer at 2.051 Å. Despite the small difference in mean Fe^{3+}-O distance, the variances of these distances are notably different between the two models. The random solution has first neighbor distance variances some three to four times larger than the locally ordered solution. The variances are produced by the deviation of the random solution from local charge balance and the accompanying bond-length adjustment to compensate for this.

The room-temperature isotropic temperature factors observed for α-$LiFeO_2$ are $B(Fe^{3+}) = 0.33$ and $B(O^{2-}) = 0.57$ Å^2 (Brunel and deBergevin, 1969). These values can be converted to Fe-O and Fe-Fe thermal bond-length variances of 0.0113 and 0.0082 Å^2, respectively, assuming that there is no correlated motion between the atoms in the bond (Böhmer and Rabe, 1978). The Debye-Waller parameters refined in EXAFS fits to the first shell for two pure α-$LiFeO_2$ samples are 0.0113(10) and 0.0120(10) Å^2. These values are consistent with the temperature factors and a small degree of static or positional disorder, i.e., with the local order model.

Second shell analysis. As judged by the calculations of Teo and Lee (1979), Li backscattering effects are probably only detectable at the lower end of the **k** range used in our analyses. Since Fe and Mg backscattering has a large amplitude in this range, any small contribution from Li is difficult to detect. It is further masked by refinement of Debye-Waller and mean free path parameters for the second shell. An attempt to measure Li backscattering amplitude by subtracting an Fe-Fe scattering function obtained from α-Fe_2O_3 resulted in weak, noisy, and inconsistent results. Future comparison of data from α- and γ-$LiFeO_2$, which have different second shell ratios of Li to Fe, may yield a detectable effect. Here, our second shell analyses neglect the presence of Li, essentially treating it as a vacancy.

In the second shell there is a marked difference between a random model, whose Fe atoms have average second shell compositions of 6Fe + 6Li, and the locally ordered model, with 4.8Fe + 7.2Li. EXAFS analysis of the second shell gives 4.61 and 4.81Fe NNN for the two samples, in excellent agreement with the locally ordered model. To obtain the highest possible precision in these second shell composition measurements, the second shell distances were held at the simulation values for refinements to locally ordered and random cases. The locally ordered distances provided consistent results. The random distances produced Fe occupancies larger than in a random case, which implies larger violations of electrostatic balance than in a random solution. Hence both refined occupancies and the consistency with simulation distances support a locally ordered configuration for α-$LiFeO_2$. Note that the constraint of total occupancy equal to 12.0 could not be imposed, as it was in the MgO-FeO analyses. The refined Debye-Waller parameter for the second shell was

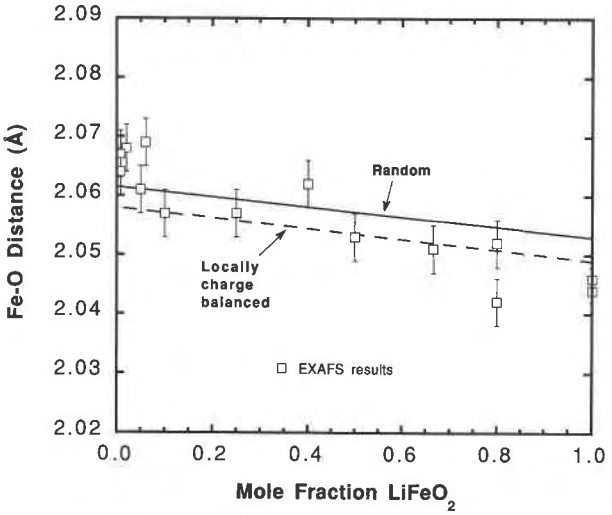

Fig. 9. First shell interatomic distances from computer simulations compared with EXAFS results for MgO–α-$LiFeO_2$. Error bars indicate 2σ.

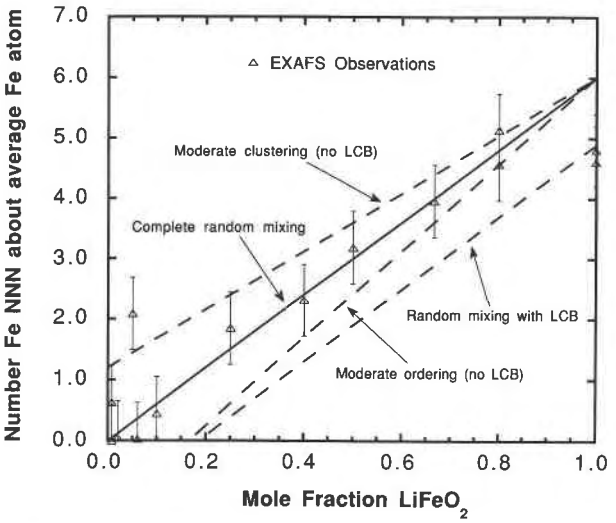

Fig. 10. NNN shell compositions for locally ordered and random MgO–α-$LiFeO_2$ from DLS simulations compared with EXAFS fit results. LCB refers to locally charge-balanced simulations. Clustering refers to a tendency to have MgO and α-$LiFeO_2$ enriched regions in the solution, and ordering refers to a tendency to have specific LiFeMg associations in the solution. Error bars indicate 2σ.

0.0104(10) Å^2. As with the first shell result, this is consistent with the locally ordered model variances and the Fe^{3+} temperature factors.

MgO-α-$LiFeO_2$

First shell analysis. The measured mean Fe^{3+}-O distances are shown in Figure 9 and compiled in Table 3. In comparison with the MgO-FeO binary system, there is a smaller change in mean Fe^{3+}-O distance, consistent with the comparatively smaller change in cell dimension from MgO to α-$LiFeO_2$. Also shown in Figure 9 are the mean Fe^{3+}-O bond lengths predicted for random and locally ordered models. The overall trend of the EXAFS data points (dotted line Fig. 9) indicates a change from random to locally charge-balanced behavior with increasing α-$LiFeO_2$ component. However, the EXAFS results are not precise enough so that we can choose unequivocally between models, especially if the anomalous behavior of the very low α-$LiFeO_2$ component samples is considered (see below). Variation in refined Debye-Waller parameters across the solid solution is about 0.002 Å^2, consistent with the random occupation simulation. The predicted maximum Debye-Waller values from the X-ray B values are 0.0108–0.0113 Å^2, compared with our fitted 0.0089–0.0120 Å^2.

Second shell analysis. In this solid solution there are three species present in the second shell around the probe Fe^{3+} species: Fe, Mg, and Li (or □). In the EXAFS analyses of these samples, the unconstrained fitting of the second shell structure function peak resulted in relative errors of up to 20%, but general agreement with the random cation simulation results. This level of imprecision, compared with the MgO-FeO series, results from the presence of three cation types in the second shell, as well as a reduced Fe content, which produces substantially less phase and amplitude variation across the solid solution.

Reduction of this error level requires the use of constraints. Here we adopt two, which are both supportable and testable and whose use results in an average relative coordination number error of only 6%. First, interatomic distances were taken from the simulation models (testing both random and locally ordered cases). Second, we assume no clustering or ordering between the MgO and α-$LiFeO_2$ components, i.e., the number of Mg cations about an average Fe^{3+} is completely dictated by the average composition. This latter constraint is thought reasonable, as clustering or ordering between these components would further hinder achievement of local charge balance (except at certain stoichiometries). In addition we find such fits to be significantly improved over constrained fits attempted with enforced clustering or ordering between MgO and α-$LiFeO_2$ components. The refinements are similarly robust with respect to the simulation-derived distance constraints. The use of distances from the locally ordered model with data well fitted by the random model produced unreasonable (very low, or negative Fe or Mg) second neighbor occupancies.

The results of the constrained second shell analyses are given in Table 4 and shown in Figure 10. The measured number of Fe,Li NNN atoms deviates from a complete random distribution ($S = 0$) by only 2.6% of total NNN atoms, on average, over the solid solution range, exclusive of the α-$LiFeO_2$ end-member. Figure 10 also shows other ordering and clustering possibilities for comparison. The moderate clustering and moderate ordering lines refer to SRO between MgO and $LiFeO_2$ components, but no local charge balancing that affects Li-Fe SRO. Debye-Waller values averaged 0.0064 Å^2 for all samples except

the end-member α-$LiFeO_2$. This value was constrained for final refinements. This is somewhat smaller than the estimated values of 0.0055–0.0082 Å^2 over the solid solution from the X-ray B values.

Sample quality, and in particular sample homogeneity, is difficult to achieve at Fe contents less than about 5% of total cations in mechanically mixed synthesis preparations. EXAFS analysis of some of the ultra-low Fe samples leads to scattered and inconsistent results, not well fitted by either a random or a locally ordered model. For example, the 5% α-$LiFeO_2$ sample has a larger than expected cell dimension (Table 1), suggesting that it is either heterogeneous or enriched in MgO. EXAFS refinements for this sample yield anomalous Fe-O distances and second shell occupancies consistent with Fe-Fe clustering. Mössbauer analyses, of this and other low-Fe samples, detailed below, further support the presence of heterogeneities possibly related to incomplete reaction or the presence of nucleated spinel clusters related to Li loss.

MgO-α-$LiFeO_2$ Mössbauer spectra

The Mössbauer spectral envelopes for the MgO–α-$LiFeO_2$ samples consist of a single doublet with relatively broad peak widths and considerable asymmetry that varies with composition. The quadrupole splitting of this envelope decreases with increasing MgO component until about 95% MgO, where with further MgO dilution the splitting increases slightly. All spectra can be fitted with one, two, or three Lorentzian line doublets with progressive improvement in the goodness of fit parameters. However, there is no evidence to suggest that any one of these fitted models has special significance over another. As practically all of the Fe^{3+} in these solutions is in octahedral coordination, the spectra must represent the distribution of slightly differing electric field gradients due to local compositional (e.g., NNN) variations. An analysis of the shape of the α-$LiFeO_2$ Mössbauer spectrum on the basis of local atomic configurations has been given by Knop et al. (1978).

For our analysis the spectra have been deconvoluted, as in the case of the MgO-FeO series. The resulting spectra show improved resolution but no evidence for the presence of discrete doublets at any composition. In the samples with highest MgO composition, the spectra can be fitted well by a single doublet of 50% Gaussian-Lorentzian character. The results of one and two doublet fits to the deconvoluted spectra appear in Table 5.

The important difference between the MgO-FeO and MgO–α-$LiFeO_2$ Mössbauer results is that even at quite low Fe concentrations the Fe^{3+} environment is not isotropic. That is, a considerable fraction of the Fe^{3+} in the latter solution has a finite quadrupole splitting. Hence there is local distortion, presumably due to the presence of other Fe^{3+} ions, Li^+ ions, or charge-compensating cation vacancies. Mössbauer investigations of Fe^{3+} doped into MgO without charge-compensating ions show similar quadrupole doublets, even at the lowest Fe^{3+} concentrations (Waychunas, 1983; Leider and Pipkorn, 1968). Those observations suggested that the cation vacancy and Fe^{3+} couple produces a quadrupole doublet splitting of 0.6–0.7 mm/s. As the quadrupole splitting is smaller in our samples, it is reasonable to conclude the presence of Li-Fe^{3+} couples, which should result in less local distortion than □-Fe^{3+} combinations. Heterogeneities in the high MgO samples could explain the larger scatter in Mössbauer results in this region and the slight increase in quadrupole splitting.

Discussion

SRO and defect arrangements in MgO-FeO solid solutions

The MgO-FeO solid solution system represents a typical homovalent substitution well suited to EXAFS study because of the difference in phase and magnitude of the backscattering amplitudes of these atoms. Our samples, synthesized and rapidly quenched from 1140 °C, have Fe-Fe NNN correlations equivalent to a random distribution ($S = 0$), with an uncertainty of about 1.4%.

The good agreement of measured EXAFS Fe-O distances with model distances simulated when random distributions are assumed further supports this conclusion. Related EXAFS analyses of alkali halide NaCl structure solid solutions (Boyce and Mikkelsen, 1984) and comparison with simulation models (Dollase, 1987) indicate analogous deviations from a Vegard model and a similar site compliance.

Although our measurements support a random distribution, it must be pointed out that nonrandom SRO could develop at lower temperatures or with slower cooling. The slight positive excess free energy of mixing in the MgO-FeO system (Hahn and Muan, 1962) indicates a clustering tendency.

With the absence of any significant clustering at high temperatures, the small Fe^{3+} component appears to have little effect on the homovalent substitution. The Fe^{3+} apparently behaves independently, although Mössbauer spectra of similar Fe-Mg ratio samples with differing Fe^{3+} contents show some broadening of the Fe^{2+} resonance (Waychunas, 1979). If the Fe^{3+} occurred only within clusters of an Fe^{3+}-rich phase, we might expect to see some differences in the EXAFS Fourier transforms between samples with low and high Fe^{3+} content, particularly in the form of the NNN shell. However, we do not observe significant differences, and no second phases were observed in XRD patterns. Hence any Fe^{3+} in these materials must exist either in solution or as extremely small clusters of a second phase. As we suggested above, that is consistent with the EXAFS results if mainly $^{[6]}Fe^{3+}$ is involved.

SRO, defect clustering, and limitations of the simulations of MgO-α-$LiFeO_2$

The heterovalent, charge-coupled substitution of Li + Fe^{3+} for 2Mg in the MgO–α-$LiFeO_2$ solid solution was chosen as a likely example of nonrandom SRO. The substantial positive volume of mixing observed in this solid

solution (Fig. 1 and Table 1) may indicate further SRO complexities. The simulations demonstrate that significant, but incomplete, local short-range order could be established at any composition in the solid solution series through a relatively small number of diffusive interchanges, each of which improves local charge balance. However, more complete ordering, for example, of the type leading from random distributions to ordered lower symmetry polymorphs of α-$LiFeO_2$ (Fayard, 1961), requires more complex, cooperative atomic rearrangements involving intermediate, charge unbalancing steps.

Our EXAFS measurements on MgO–α-$LiFeO_2$ solid solutions show composition-dependent SRO. For end-member α-$LiFeO_2$, the observed degree of SRO is in good agreement with the locally short-range ordered computer models. It is also consistent with the degree of SRO observed by means of X-ray diffuse intensity measurements in cubic α-$LiFeO_2$ quenched from temperatures somewhat below those used here (Brunel and deBergevin, 1968, 1969). Second shell NNN EXAFS results for the MgO-bearing solid solution, however, are more closely in agreement with a random distribution of all cations about the probe Fe^{3+}. The apparent change to random behavior at moderate MgO concentration is perhaps not surprising, when one considers that order-disorder transition temperatures in the analogous system MgO-Li_2TiO_3 (Castellanos and West, 1979) decrease rapidly with increasing MgO component.

The change from local ordering to near random distributions appears to take place in the vicinity of 20 mol% MgO content. The nearly random SRO could be explained as a kinetic effect due to the driving force for local charge balance being strong at α-$LiFeO_2$ but rapidly reduced by the dilutant effect of MgO.

It is conceivable, though to date no one has reported such an observation, that long-range ordered intermediate members of this solid solution could be formed near specific compositions such as Mg_6LiFeO_8, which could show a cation arrangement analogous to that in the ordered vacancy structure of Mg_6MnO_8 (Kasper and Prener, 1954). With the low temperature (about 600 °C) for the long-range order-disorder transformation of $LiFeO_2$ and the likely dilution effects of Mg, ordering temperatures might be so low that long-range ordering is kinetically unattainable. On the basis of the considerable excess volume of mixing, it is rather more likely that the system has a binary loop stability region in T-X space, with the long-range order-disorder transition in the $LiFeO_2$ end-member dropping rapidly in temperature with MgO content.

The use of EXAFS with computer simulations for structure analysis

Our results demonstrate that the determination of mixed cation shell compositions can be improved over that of previous studies with the use of separately determined parameters such as interatomic distances. Nearly as important for robust analysis are the use of suitable constraints, such as total coordination (=12 in the NaCl structure second shell), and restraints, such as no coordination number being allowed to become negative. As a further test of our method, some refinements of the MgO-FeO NNN compositions were attempted without any constraints, fixed parameters, or restraints. The results still agreed with the random model, but relative errors increased about threefold. Our simulations thus allow us to move from qualitative to quantitative determination of the SRO parameters.

Applications to other systems

Similar simulations could be performed on almost any system for which appropriate well-defined interatomic distances are known independently. In systems with more complex charge-coupled substitutions, e.g., solutions where two or more crystallographic sites are involved, as in perovskite of type $KTa^{5+}O_3$-$Pb^{2+}Ti^{4+}O_3$, the method of cation exchange used to produce charge balance may require modification. A more severe problem occurs if the requirements of charge balancing and structure topology become inconsistent, i.e., the simulation produces local charge balance only at the cost of a highly improbable structure distortion. Finally, the effect of simulated temperature must be considered to produce results that are physically more meaningful.

The EXAFS analysis requires cations with differing amplitude functions and phase functions over the k range collected. Cations differing by only a few atomic numbers are difficult to resolve because of very similar k-space functions. Despite these limitations, the present method represents the most practical approach for examining SRO phenomena in many ceramic and mineral solid solutions, especially in cases where the ions of interest are at low total concentration.

Acknowledgments

G.A.W. is thankful for support from the NSF-MRL Program through the Center for Materials Research at Stanford University. G.A.W. and W.A.D. are grateful to Friedrich Seifert and the Bayerisches Geoinstitut for their hospitality and support during the early stages of manuscript preparation, while many of the calculations were being made. EXAFS data were collected at SSRL, which is supported by the Department of Energy. Helpful reviews by Ben Burton, Mike Fleet, and Paul Flinn are gratefully acknowledged.

References cited

Barron, T.J.K. (1977) Room temperature Debye-Waller factors of magnesium oxide. Acta Crystallographica, A33, 602.

Bessiere, M., Dartyge, E., and Lefebvre, S. (1986) Study of short range order in Au_3Cu by EXAFS. Journal de Physique, C8, 47, 1033–1036.

Böhmer, W., and Rabe, P. (1978) Temperature dependence of the mean square relative displacements of nearest-neighbor atoms derived from EXAFS spectra. Journal of Physics C: Solid State Physics, 12, 2465–2474.

Boyce, J.B., and Mikkelsen, J.C. (1984) Local structure of pseudobinary alloys. Proceedings in Physics, 2, 427–431.

Brown, G.E., Jr., Calas, G., Waychunas, G.A., and Petiau, J. (1988) X-ray absorption spectroscopy: Applications in mineralogy and geochemistry. In Mineralogical Society of America Reviews in Mineralogy, 18, 431–512.

Brown, I.D., and Altermatt, D. (1985) Bond-valence parameters obtained from a systematic analysis of the inorganic crystal structure database. Acta Crystallographica, B41, 244–247.

Brunel, M., and deBergevin, F. (1968) Structure de la phase Q_{II} (ou β) du ferrite de lithium $FeLiO_2$: Exemple d'antiphase périodique. Journal of Physics and Chemistry of Solids, 29, 163–169.

——— (1969) Ordre à courte distance, déplacements locaux des ions et énergie électrostatique dans $FeLiO_2$. Journal of Physics and Chemistry of Solids, 30, 2011–2021.

Burnham, C.W. (1985) Mineral structure energetics and modeling using the ionic approach. In Mineralogical Society of America Reviews in Mineralogy, 14, 347–388.

Castellanos, M., and West, A.R. (1979) Order-disorder phenomena in oxides with rock salt structures: The system Li_2TiO_3-MgO. Journal of Materials Science, 14, 450–454.

Claeson, T., and Boyce, J.B. (1984) Order-disorder transformation in Au-Cu alloys studied by extended X-ray-absorption fine structure. Physical Review B, 29, 1551–1557.

Darken, L.S., and Gurry, R.W. (1945) The system iron-oxygen. I. The wüstite field and related equilibria. Journal of the American Chemical Society, 67, 1398–1412.

——— (1946) The system iron-oxygen. II. Thermodynamics of liquid oxide and other phases. Journal of the American Chemical Society, 68, 796–816.

deFontaine, D. (1971) The number of independent pair-correlation functions in multicomponent systems. Journal of Applied Crystallography, 4, 15–19.

Dollase, W.A. (1980) Optimum distance model of relaxation around substitutional defects. Physics and Chemistry of Minerals, 6, 295–304.

——— (1987) Distribution of interatomic distances in solid solutions of the NaCl type. Zeitschrift für Kristallographie, 179, 215–231.

Dowty, E., and Lindsley, D.H. (1973) Mössbauer spectra of synthetic hedenbergite-ferrosilite pyroxenes. American Mineralogist, 58, 850–868.

Fayard, M. (1961) Sur les phénomènes ordre-désordre dans l'oxyde mixte $LiFeO_2$ et sur les propriétés de ses solutions solides avec quelques oxydes du type NaCl. Annales de Chimie, 6, 1279–1337.

Finnerty, A.A., Waychunas, G.A., and Thomas, W.M. (1978) The preparation of starting mixes for mineral syntheses by a freeze-dry technique. American Mineralogist, 63, 415–418.

Hahn, W.C., and Muan, A. (1962) Activity measurements in oxide solid solutions: The system "FeO"-MgO in the temperature interval 1100 to 1300C. Transactions of the Metallurgical Society of AIME, 224, 416–420.

Hauck, J. (1980) Short-range order and superstructures of ternary oxides AMO_2, A_2MO_3 and A_5MO_6 of monovalent A and multivalent M metals related to the NaCl structure. Acta Crystallographica, A36, 228–237.

Hentschel, B. (1970) Stoichiometric FeO as metastable intermediate of the decomposition of wüstite at 225 C. Zeitschrift für Naturforschung, 25A, 1996–1999.

Kasper, J.S., and Prener, J.S. (1954) The crystal structure of Mg_6MnO_8. Acta Crystallographica, 7, 246–248.

Knop, O., Ayasse, C., Carlow, J.S., Barker, W.W., Woodhams, F.W., Meads, R.E., and Parker, W.G. (1978) Origin of the quadrupole splitting in the Mössbauer ^{57}Fe spectrum of cubic (disordered) $LiFeO_2$. Journal of Solid State Chemistry, 25, 329–346.

Koch, F., and Cohen, J.B. (1969) The defect structure of $Fe_{1-x}O$. Acta Crystallographica, B25, 275–287.

Kurash, V.V., Goldanskii, V.I., Malysheva, T.V., Urusov, V.S., Kuznetsov, L.M., and Moskovkina, L.A. (1971) Mössbauer study of the solid solutions MgO-$Fe_{1-x}O$. Izvestiya Akademie Nauk SSSR, Neorganicheskie Materialy, 7, 1574–1580.

Leider, H.R., and Pipkorn, D.N. (1968) Mössbauer effect in MgO:Fe^{2+} low temperature quadrupole splitting. Physical Review, 165, 494–502.

Lytle, F.W., Sandstrom, D.R., Marques, E.C., Wong, J., Spiro, C.L., Huffman, G.P., and Huggins, F.E. (1984) Measurement of soft X-ray absorption spectra with a fluorescence ion chamber detector. Nuclear Instruments and Methods, 226, 542–548.

Manceau, A., Bonnin, D., Stone, W.E., and Sanz, J. (1990) Distribution of Fe in the octahedral sheet of trioctahedral micas by polarized EXAFS: Comparison with NMR results. Physics and Chemistry of Minerals, 17, 363–370.

Meier, W.M., and Villiger, H. (1969) Methode der Abstandnerfinerung zur Bestimmung der Atomkoordinaten idealisierter Geruststrukturen. Zeitschrift für Kristallographie, 129, 411–423.

Osborne, M.D., Fleet, M.E., and Bancroft, G.M. (1984) Next-nearest neighbor effects in the Mössbauer spectra of (Cr,Al) spinels. Journal of Solid State Chemistry, 53, 174–183.

Phillips, B., and Muan, A. (1962) Phase equilibria in the system MgO-FeO-Fe_2O_3 in the temperature range 1400 to 1800 C. Journal of the American Ceramic Society, 45, 588–598.

Riedel, E., and Karl, R. (1980) Mössbauer studies of thiospinels. I. The system $FeCr_2S_4$-$FeRh_2S_4$. Journal of Solid State Chemistry, 35, 77–82.

Seifert, F. (1983) Mössbauer line-broadening in aluminous orthopyroxenes: Evidence for next-nearest-neighbor interactions and short-range order. Neues Jahrbuch für Mineralogie, 148, 141–162.

Steger, J., and Kostiner, E. (1973) Mössbauer and magnetic investigation of point defects in iron-doped cadmium fluoride. Journal of Chemical Physics, 58, 3389–3400.

Teo, B.K. (1986) EXAFS: Basic principles and data analysis. Springer-Verlag Inorganic Chemistry Concepts, 9, 349 p.

Teo, B.K., and Lee, P.A. (1979) Ab initio calculations of amplitude and phase functions for extended X-ray absorption fine structure spectroscopy. Journal of the American Chemical Society, 101, 2815–2832.

Ure, M.C.D., and Flinn, P.A. (1971) A technique for removal of the "blackness" distortion of Mössbauer spectra. Mössbauer Effect Methodology, 7, 245–262.

Vinze, I. (1982) Fourier evaluation of broad Mössbauer spectra. Nuclear Spectroscopy and Nuclear Instruments and Methods, 199, 247–262.

Warren, B.E. (1968) X-ray diffraction, 381 p. Addison-Wesley, Reading, Massachusetts.

Waychunas, G.A. (1979) Mössbauer, X-ray, optical and chemical study of cation arrangements and defect association in $Fm3m$ oxides in the system periclase-wüstite-lithium ferrite, 456 p. Ph.D. thesis, University of California, Los Angeles.

——— (1983) Mössbauer, EXAFS and X-ray diffraction study of Fe^{3+} clusters in MgO:Fe and magnesiowüstite $(Mg,Fe)_{1-x}O$: Evidence for specific cluster geometries. Journal of Materials Science, 18, 195–207.

Waychunas, G.A., Brown, G.E., and Apted, M.J. (1986) X-ray K-edge absorption spectra of Fe minerals and model compounds. II. EXAFS. Physics and Chemistry of Minerals, 13, 31–47.

Manuscript received June 26, 1992
Manuscript accepted November 12, 1993